Open Access Online Journal on Astronomy and Astrophysics

Acta Astrophysica Taurica

www.astrophysicatauricum.org

Acta Astrophys. Tau. 5(3), 18–26 (2024)

Identifying objects of the optical range in the regions of hard radiation near red dwarf stars

A.A. Shlyapnikov

Crimean Astrophysical Observatory, Nauchny 298409
e-mail: aas@craocrimea.ru

Received 5 November 2021

ABSTRACT

We analyze the localization regions of TeV gamma-ray sources in the X-ray and optical spectral ranges. The angle distances from the position of maxima in the distribution of high-energy fluxes to the probable candidates for identification with red dwarfs are indicated. Possible identifications of fainter TeV sources and other field objects are also considered.

Key words: X-ray and gamma-ray sources, stars – variable and peculiar

1 Introduction

The problem of identifying the first "discrete" sources of hard radiation (10^{-8}–10^{-11} erg ≈ 0.6 MeV−0.6 keV) in the optical range has historically been associated with low accuracy in determining their coordinates. Thus, the first discrete X-ray source was detected in 1962 in the Scorpius constellation by a detector installed on a rocket and was designated as Sco X-1 (Giacconi et al., 1962). After refining its coordinates (Gursky et al., 1966), it was identified with an accuracy of about 1′ with a star of $V \approx 13^{m}$, which had an ultraviolet excess in 1966 (Sandage et al., 1966). Four years have passed since the discovery of the discrete X-ray source up to its identification in the optical spectral range.

The history of identifying sources in the gamma-ray spectral range turned out to be more dramatic. The most characteristic example is a search for sources of gamma-ray bursts (GRBs) in other spectral ranges.

Information on observations of 16 GRBs was first published in 1973 (Klebesadel et al., 1973). They were detected by four Vela series satellites[1] between July 1969 and July 1972 in the energy range of 0.2–1.5 MeV, had durations from 0.1 to more than 30 seconds and time-integrated flux densities from $\sim 10^{-5}$ to $\sim 2 \times 10^{-4}$ erg × s × cm^{-2}. The arrival direction of GRBs was associated with neither the Earth (the satellites recorded gamma-ray radiation caused by testing nuclear weapon) nor the Sun.

Only on February 1997, 28.123620 UT, 24 years later, the BeppoSAX satellite[2] detected a multi-peaked GRB with a duration of about 80 seconds. The image obtained with the Wide-Field Camera (WFC) in the gamma-ray range allowed the preliminary coordinates of the burst to be determined as R.A. = $5^{h}01^{m}57^{s}$ and Decl. = +11°46′.4 for the epoch 2000.0 with an error of 3′ (Costa et al., 1997). After 8 hours, thanks to pointing the Narrow Field Instrument (NFI) to the burst region, it was possible to improve the GRB coordinates. A triangulation of observations from the BeppoSAX and Ulysses[3] satellites allowed determining the coordinates by which an optical afterglow, or an optical transient, was discovered. A fading source was found by comparing observations obtained with the William Herschel Telescope[4] and the Isaac Newton Telescope[5] (Groot et al., 1997). Further observations with the Hubble Space Telescope[6] revealed not only a fading afterglow but also a possible host galaxy of the optical transient (Sahu et al., 1997). Thus, the "Era of Afterglows" for GRBs started. Some of the afterglows were identified as supernovae, while the nature of others remains unknown to this day.

The situation with identifying sources of hard radiation in the optical range has changed dramatically after the launch of the CGRO, Chandra, eROSITA, Fermi, GRANAT, INTEGRAL, MAXI, ROSAT, Rossi-XTE, XMM-Newton space observatories and the creation of the InterPlanetary Network (IPN)[7]. More information on the mentioned projects can be found at link.

[1] https://heasarc.gsfc.nasa.gov/docs/heasarc/missions/vela5a.html
[2] https://heasarc.gsfc.nasa.gov/docs/sax/sax.html
[3] https://web.archive.org/web/20110806115817/http://ulysses.jpl.nasa.gov/
[4] http://www.ing.iac.es/astronomy/telescopes/wht/
[5] http://www.ing.iac.es/astronomy/telescopes/int/
[6] https://www.nasa.gov/mission_pages/hubble/about
[7] https://heasarc.gsfc.nasa.gov/docs/heasarc/missions/ipn.html

Despite the high accuracy of localizing sources of hard radiation, which amounts to angular minutes, not all detected sources were identified in the optical spectral range. This does not allow a detailed study of their nature.

While the accuracy in determining the coordinates for objects of hard radiation has been improved in space observations, the situation with ground-based observations at the telescopes detecting Cherenkov radiation caused by gamma-ray fluxes in the Earth's atmosphere is different. When covering a sky area of several degrees, the angular resolution of Cherenkov telescopes ranges from 15′ to 2°, which makes it very problematic to identify gamma-ray sources in the optical spectral range.

This paper presents an analysis of localization regions of six TeV gamma-ray sources in the optical spectral range. The angular distances from the positions of maxima in the distribution of high-energy fluxes to probable candidates for identification with red dwarfs are indicated. Possible identifications of fainter gamma-ray sources with other objects are also considered.

2 Hard radiation from the Sun and stars

The quiet Sun is a source of soft X-ray radiation generated in the corona. At photon energies below 10^{-9} erg, the flux decreases sharply and is practically not observed in the gamma-ray range. This was discovered during the first experimental and theoretical studies of hard radiation from the Sun (Peterson, Winckler, 1959). During solar flares, photon energies can vary from hundreds of keV to tens of MeV (Holt, Ramaty, 1969). It is important to note a temporal correlation between hard X-ray and microwave radiation. A search for radio impulses coinciding in time with observations in the hard spectral range (Baird et al., 1975) did not yield results. However, an upper limit on radio radiation was obtained, excluding stellar flares as a source of gamma-ray bursts on condition that they are similar to solar flares but larger in scale (Cavallo, Jelley, 1975).

As observational equipment improved, the problem of identifying hard radiation from stars, particularly dwarf stars in the lower part of the main sequence, developed. In the GTSh10 catalog of 5535 stars with solar-type activity (Gershberg et al., 2011), X-ray radiation was detected in about 2000 objects. Most of them exhibit optical flares with significant amplitudes.

A unique event was recorded for the red dwarf DG CVn (D'Elia et al., 2014). On April 23, 2014 at 21:07:08 UT, the Burst Alert Telescope (BAT) on board the Swift space observatory detected a flare in the 15–50 keV energy range, which lasted for 64 seconds. Further X-ray observations allowed the flare coordinates to be refined to 4″.9 and the object to be identified with the flaring star DG CVn of spectral type M4.0V.

The relevance of studying the flaring activity of red dwarfs is due to the discovery of exoplanets for several thousand stars, many of which are stars with solar-type activity (Gorbachev et al., 2019). This problem is discussed in detail in Caballero-García et al. (2016).

3 Observations of red dwarf regions in the TeV range

The first observations of regions containing red dwarfs in the TeV range with energies of $\sim 10^{12}$ eV were obviously performed at the Crimean Astrophysical Observatory in 1994 (Alekseev et al., 1995). During parallel observations of EV Lac in the optical range with the AZT-11 telescope and the GT-48 Cherenkov telescope over several nights, time-correlated events were detected in the optical and gamma-ray ranges. The most statistically reliable result in the TeV range was obtained shortly before an optical flare on August 31, 1994 at 19:40 UT. Considering the mismatch between the coordinates of the flare and EV Lac by 0°.6, the authors reported on a possible connection between the gamma-ray flare and the flare in the optical range.

The articles "Galactic cosmic rays: The first detection of TeV gamma-ray emission from red dwarfs" and "A new type of galactic cosmic ray sources" (Sinitsyna et al., 2019, 2020) present data from long-term observations within the SHALON experiment aimed at searching for emission from stars – active red dwarfs with intensities above 800 GeV. All objects are located at angular distances of less than 5° from the observed program sources of TeV emission (Tycho's supernova remnant, the Crab Nebula, 4C+41.63, and Cyg X-3). Since the field of view of the telescope within the SHALON experiment is larger than 8°, eruptive (Er) and/or flaring (Fl) stars, such as V388 Cas (Er), V1589 Cyg (Fl/Er), GJ 1078 (Fl), GL 851.1, V780 Tau (Fl/Er), and V962 Tau (Er) are simultaneously captured in the area when observing program objects.

Table 1.

Object	X-ray source	Object	X-ray source
V388 Cas	1RXS J010318.0 + 622146	GL 851.1	–
V1589 Cyg	2RSX J204249.0 + 412246	V780 Tau	2RXS J054025.1 + 244839
GJ 1078	1RXS J052327.7 + 222649	V962 Tau	2RXS J054552.1 + 225248

Sinitsyna et al. (2020) present the identification of their own observations in the X-ray spectral range with the objects listed in Table 1. Unfortunately, the authors did not combine the obtained data, presented in the form of isophotes, with optical images of the studied regions and did not carry out the identification of potential sources in the field.

4 Optical identifications, X-ray sources, and possible candidates for TeV emission

To perform the identification of images of TeV emission sources in the optical spectral range, the interactive sky atlas Aladin (Bonnarel et al., 2000) was used with loadable databases supported by the Strasbourg Astronomical Data Center.

The main data on the identified stars are presented in Table 2.

The first column of the table shows the star designation according to Sinitsyna et al. (2020); the second column contains the main designation according to SIMBAD. The third and fourth columns contain the equatorial coordinates of objects for the epoch 2000. The fifth and sixth columns show

Table 2.

Object	SIMBAD	R.A. (2000)	Decl. (2000)	pmRA (mas)	pmDE (mas)	Type	B (mag)	V (mag)	Sp. type	Dist.
V388 Cas	Wolf 47	01 03 19.83	+62 21 55.8	730.74	86.352	Er	15.46	13.78	M5V	15″
V1589 Cyg	V* V1589 Cyg	20 42 49.16	+41 23 00.0	67.3	−31.1	Fl/Er	15.29	13.59	–	15″
GJ 1078	G 85-69	05 23 49.05	+22 32 38.8	236.0	−300.0	Fl	17.35	15.52	M4.5V	9″
GL 851.1	BD+30 4633	22 12 06.42	+31 33 41.1	−344	−418.8	Fl	11.43	10.15	K5V/dM0e	21″
V780 Tau	G 100-28	05 40 25.73	+24 48 07.8	107.0	−376.0	Fl/Er	16.74	14.94	M7V	10″
V962 Tau	V* V962 Tau	05 45 51.94	+22 52 47.4	0.142	−9.959	Er	13.5	–	–	10″

the proper motions of the stars in right ascension and declination in angular milliseconds per year. The seventh column indicates the variability type of the star. The eighth and ninth columns contain the brightness in the *B* and *V* bands. The tenth column provides information on the spectral type of the star, and the eleventh column shows the angular distance from the maximum flux in the gamma-ray range to the optical image of the star.

5 The V388 Cas region

The maximum gamma-ray flux (MGF) is located at a distance of 15 arcsec from the optical position of V388 Cas (Fig. 1). In the figure, the maximum corresponds to the reddest shade of the isophote and almost coincides with the red marker and circle of the same color. Obviously, this circle limits the error radius (ER) in determining the coordinates of the X-ray source, which Sinitsyna et al. (2020) designated as the position of 1RXS J010318.0+622146. However, the actual position of the source is slightly lower, at a distance of 23″ (green circles with a smaller radius of 1 × ER and a larger radius of 3 × ER, marked with numbers 2 and 3).

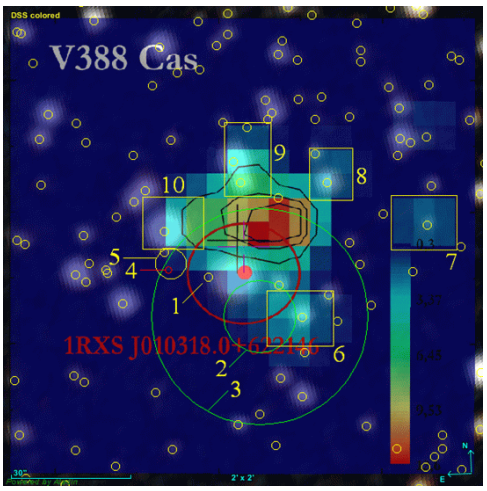

Fig. 1. Combined optical (DSS colored) and TeV images of the V388 Cas region. The positions and ER of X-ray sources are marked with circles, while potential optical identifications are indicated by rectangles. Small yellow circles denote stars from the GAIA DR2 catalog.

The red circle with ER = 0″.8 (number 4) indicates the position of the X-ray source 4XMM J010321.3+622157 (Webb et al., 2020) recorded by the XMM-Newton telescopes and located at a distance of 28″ from the MGF. The yellow circle with ER = 3″.9, at a distance of 27″ (number 5), indicates the position of the X-ray source 2SXPS J010321.2+622159 (Evans et al., 2020) observed by the Swift observatory.

Small yellow circles in the figure show the positions of stars from the GAIA DR2 catalog (Gaia Collaboration et al., 2018). Number 1 corresponds to V388 Cas. The difference in the position of the star according to GAIA data and in the optical image is due to the significant proper motion (730.740 in right ascension and 86.352 in declination in angular milliseconds per year, respectively).

Several regions in the vicinity of V388 Cas are noteworthy, where faint gamma-ray sources are located, bounded by yellow rectangles (marked with numbers 6, 7, 8, 9, and 10). Inside these regions, there are objects from the GAIA DR2 catalog with the following characteristics (Table 3).

Table 3 lists the numbers of rectangles with faint gamma-ray sources in which objects were found. Number 1 corresponds to V388 Cas. Numbers 9 ↑ and 9 ↓ belong to the upper and lower objects in the ninth rectangle. The columns further show the coordinates of the objects, parallax, proper motion in right ascension and declination according to the GAIA DR2 catalog, the average stellar magnitudes in the G, G_{BP}, and G_{RP} bands in the GAIA photometric system, effective temperature, radii, and luminosities of the stars compared to the solar values.

It should be noted that according to the data from the second ROSAT source catalog (Boller et al., 2016), the object 1RXS J010318.0+622146 is associated with the X-ray source 2RXS J010318.3+622140 and exhibits weak variability (Fig. 2).

It should also be noted that the X-ray source 2SXPS J010321.2+622159 has a closer location to object 10 from Table 3 than to V388 Cas. In the case of using the 3 × ER criterion, it unambiguously falls into the field of the X-ray source.

6 The V1589 Cyg region

The coordinates given in Sinitsyna et al. (2020) differ by 1 degree (Fig. 3a) from those of the object in the SIMBAD database (Wenger et al., 2000).

The star is located in the upper part of the image, and the area of the recorded gamma-ray emission is in the lower part of the figure. When the coordinates of the TeV image are aligned with the coordinates of V1589 Cyg, the maxi-

Table 3.

No.	R.A. (2000)	Decl. (2000)	Plx	pmRA	pmDE	G	G_{BP}	G_{RP}	T_{eff}	Rad	Lum
1	015.83942594	+62.36588063	101.6371	730.740	86.352	11.9238	13.9068	10.6032	3346.00	–	–
6	015.81867355	+62.36274707	0.4845	−1.450	−0.828	17.8200	18.5362	16.9453	–	–	–
7	015.79997556	+62.36915143	−0.0123	0.921	0.653	19.6506	20.5764	18.5647	–	–	—
8	015.81488911	+62.37208876	0.3020	−1.116	−0.125	16.5141	17.8314	15.3511	3670.99	–	–
9 ↑	015.82903889	+62.37352009	1.5970	2.231	−7.581	15.1327	15.7619	14.3744	4547.58	0.92	0.326
9 ↓	015.82802289	+62.37205461	0.6506	8.320	−2.823	16.7946	17.5051	15.9437	4312.85	1.23	0.470
10	015.83925097	+62.36866398	0.3280	−3.790	−0.808	13.5627	14.4896	12.6116	3945.89	14.34	44.925

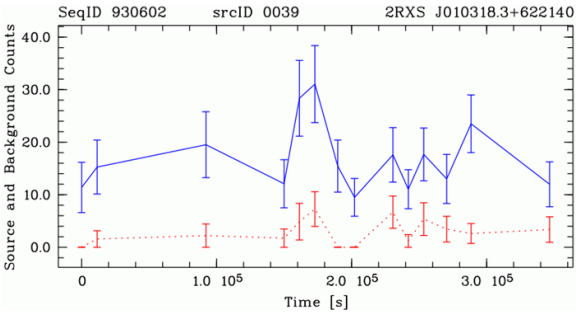

Fig. 2. Light curve of the object 2RXS J010318.3+622140 in the X-ray spectral range. The axes show time from the start of observations in seconds and detector counts for the source (blue curve) and background (red curve). Measurement errors are indicated.

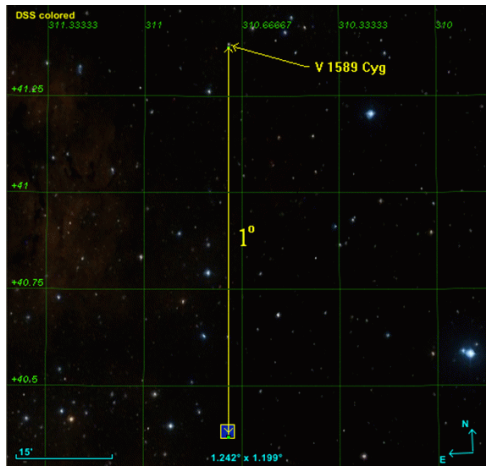

a)

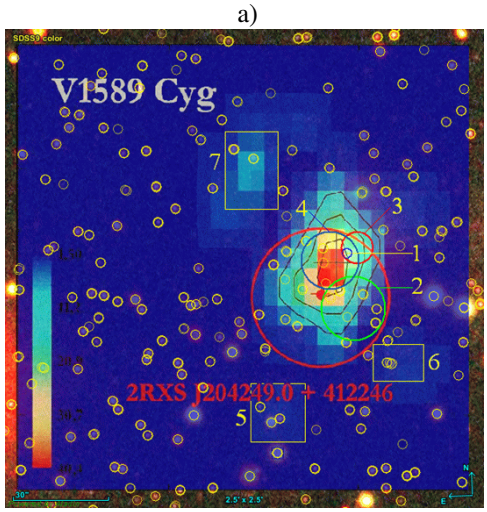

b)

Fig. 3. a) Real position of V1589 Cyg (in the upper part of the figure) and the position of the TeV source according to the coordinates from Sinitsyna et al. (2020). b) Combined optical (SDSS9 color) and TeV images of the V1589 Cyg region. Circles indicate the positions and ER of X-ray sources, rectangles indicate regions with possible optical identifications. Small yellow circles mark stars from the SDSS DR12 catalog.

mum flux in the gamma-ray range is located at a distance of ~15 arcsec from the optical position of the star (Fig. 3b).

The numbers in Fig. 3b are denoted as follows: 1 – the position of V1589 Cyg according to the coordinates for the epoch 2000 (small blue circle); 2 – green circle corresponding to 1 × ER of the source 1RXS J204249.0+412242; 3 – small red circle corresponding to 1 × ER of the source XMMSL2 J204248.9+412302 (XMM-SSC, 2017); 4 – blue circle – the error region of the position of the object 1SWXRT J204249.6+412257 from the Swift observatory catalog (D'Elia et al., 2013). Small yellow circles mark stars from the SDSS DR12 catalog (Alam et al., 2015).

The large red circle is the position and ER of the source 2RXS J204249.0+412245 from Sinitsyna et al. (2020). It should be noted that the X-ray sources XMMSL2 J204248.9+412302 and 1SWXRT J204249.6+412257 are closer in coordinates to V1589 Cyg and have a smaller ER.

The objects located in the regions of weak gamma-ray emission (Fig. 4), designated by yellow rectangles with numbers 5, 6, and 7 in Fig. 3b, are of interest. The maximum flux in these regions exceeds the background level by more than 3 times for regions 5 and 6, and by about 7 times for region 7 (the flux was estimated using the isophote intensity scale shown in the left part of the figure). Some of the objects in these regions (Table 4) may be sources of gamma-ray emission.

Table 4 lists the numbers of rectangles with faint gamma-ray sources and the corresponding object numbers in these regions. The columns further show the coordinates of the objects, the number of observations, the average values of stellar magnitudes and their determination errors in the u, g, r, i, z bands of the SDSS DR12 catalog color system. The last column shows the approximate averaged spectral type of the objects found by color indices (Pecaut, Mamajek, 2013; Mamajek, 2019).

All objects in the regions, except for 6.1, are classified in the SDSS DR12 catalog as stars and have good observation quality. Object 6.1 has two classifications, as a star and as a galaxy, based on modeling the photometric profile of its

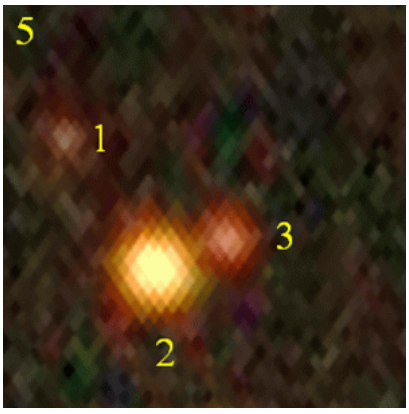

a) Map of region 5

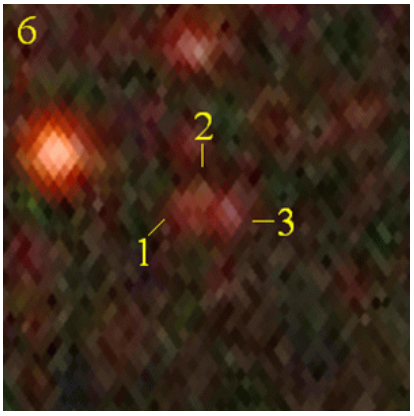

b) Map of region 6

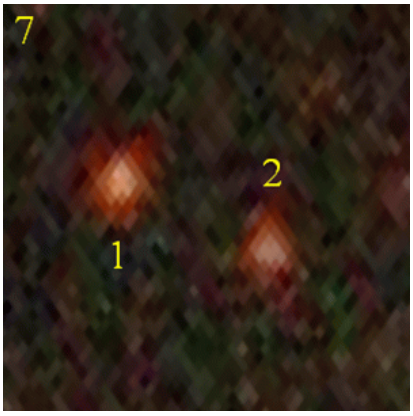

c) Map of region 7

Fig. 4.

Table 4.

No.	R.A. (2000)	Decl. (2000)	n	u	er_u	g	er_g	r	er_r	i	er_i	z	er_z	Sp
5.1	310.71493530	+41.36992645	3	24.966	0.836	25.037	0.585	23.865	0.474	22.070	0.161	20.869	0.227	K5
5.2	310.71368408	+41.36857986	4	25.075	0.905	21.431	0.052	19.367	0.014	18.330	0.010	17.610	0.018	M5
5.3	310.71267700	+41.36889267	3	24.885	0.898	24.976	0.548	23.218	0.312	21.014	0.068	19.570	0.077	M3
6.1	310.70025635	+41.37376785	2	24.338	0.873	24.603	0.590	23.691	0.572	21.437	0.131	20.042	0.160	K2
6.2	310.69989600	+41.37380900	1	25.673	0.884	26.649	0.382	25.641	0.626	23.606	0.801	20.507	0.256	K5
6.3	310.69964600	+41.37366486	2	24.700	0.937	24.490	0.482	24.584	0.618	22.528	0.273	20.879	0.231	A2
7.1	310.71801758	+41.39233780	4	25.696	0.720	24.912	0.580	22.309	0.154	20.643	0.055	19.247	0.067	M6
7.2	310.71572876	+41.39153671	3	24.945	0.779	24.820	0.564	22.899	0.233	21.180	0.075	19.726	0.087	M4

image. All three objects in region 6, considering their close location, are presumably a single extended object – a galaxy, and the classification of objects 2 and 3 is erroneous.

7 The GJ 1078 region

The X-ray source 1RXS J052327.7+222649 (Voges et al., 2000), presented in Sinitsyna et al. (2020) as a possible identification for GJ 1078, is located at a distance of more than 7 arcmin from the maximum of the TeV image and has an error radius significantly smaller than that given in the publication. Figure 5 shows the position of 1RXS J052327.7+222649 and the corresponding ER (12″) (green circle) in the lower right part of the image.

A possible identification for the X-ray source 1RXS J052327.7+222649 is a star falling within the ER, GAIA DR2 3414565834307772672, with characteristics listed in Table 5.

The table lists the star's coordinates, its parallax, proper motion in right ascension and declination in standard units, stellar magnitudes in the G, G_{BP}, G_{RP} bands in the photometric system of the GAIA DR2 catalog, and the effective temperature (K).

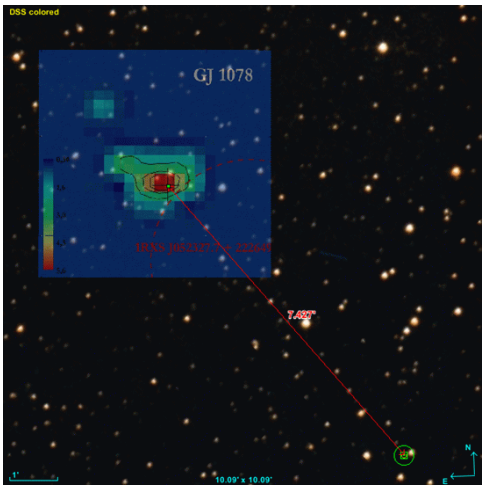

Fig. 5. Combined optical (DSS colored) and TeV images of the GJ 1078 region.

The object 1RXS J052327.7+222649, listed in the ROSAT source catalog (Boller et al., 2016) as 2RXS

Table 5.

R.A. (2000)	Decl. (2000)	Plx	pmRA	pmDE	G	G_{BP}	G_{RP}	T_{eff}
080.86267583	+22.44798972	10.0892	−21.366	−28.036	14.3127	15.6859	13.1702	3887.82

Table 6.

No.	R.A. (2000)	Decl. (2000)	Plx	pmRA	pmDE	G	G_{BP}	G_{RP}	T_{eff}	Rad	Lum
4.1	080.95877765	+22.53166155	0.4863	−0.857	−2.930	19.2419	20.3034	18.1495	–	–	–
4.2	080.95869733	+22.53614840	1.6889	−1.487	0.121	19.8610	20.4998	18.8138	–	–	–
4.3	080.95720994	+22.53378669	0.8952	5.567	−10.956	20.4132	21.0040	19.0972	–	–	–
4.4	080.95637812	+22.52918229	0.4649	−0.462	−2.973	19.1219	20.0388	18.1138	–	–	–
4.5	080.95624474	+22.53162562	0.6151	−1.024	−2.809	15.6819	16.4185	14.8271	4430.25	2.00	1.388
4.6	080.95490905	+22.53444779	0.6055	0.384	−8.921	16.7066	17.6193	15.7507	3883.25	–	–
5.1	080.97186813	+22.55128457	0.8428	2.418	−3.582	16.2663	17.0784	15.3653	4008.50	1.53	0.543
5.2	080.97147333	+22.54862508	0.1456	0.231	−1.259	19.3775	20.1277	18.4256	–	–	–
5.3	080.96782341	+22.54390129	−0.0681	−0.261	−0.314	19.5618	20.4901	18.5803	–	–	–
6.1	080.97919404	+22.56397196	0.5140	1.560	−5.213	20.5542	20.9304	19.2965	–	–	–
6.2	080.97843061	+22.56320793	0.7603	0.791	−0.843	19.4131	20.0881	18.3599	–	–	–
6.3	080.97714800	+22.56847806	0.0570	1.022	−0.240	20.0700	20.9232	18.9711	–	–	–
6.4	080.97603549	+22.56508820	0.1715	1.641	−1.392	17.6060	18.5273	16.6349	–	–	–
7	080.95844612	+22.54333320	0.4040	−1.151	−2.167	16.7120	17.4675	15.8276	4239.00	–	–

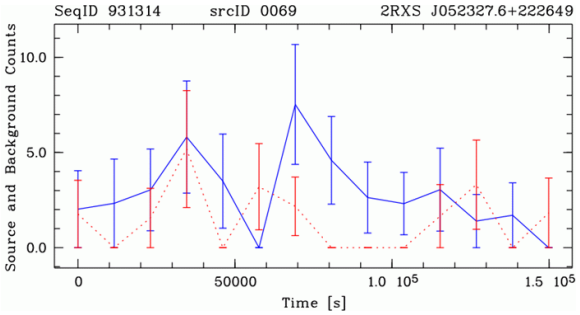

Fig. 6. X-ray light curve of the object 2RXS J052327.6+222649. The axes show time from the start of observations in seconds and detector counts for the source (blue curve) and background (red curve). Measurement errors are indicated.

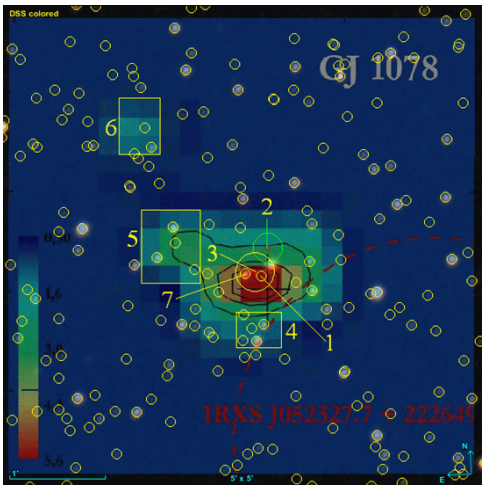

Fig. 7. Combined optical (DSS colored) and TeV images of the GJ 1078 region with indicated objects and regions for which identification was performed.

J052327.6+222649, demonstrates insignificant variability at the background level in the X-ray range, as shown in Fig. 6.

Consider in detail the TeV image region for GJ 1078 from Sinitsyna et al. (2020), shown in Fig. 7. The numbers are denoted as follows: 1 – the position of GJ 1078 from the GAIA DR2 catalog (the star is located at a distance of 9″ from the maximum of the TeV source); 2 – X-ray source 1RXH J052349.0+223251 (RST, 2000) with an ER of 9″ (green circle); 3 – X-ray source 1RXH J052349.5+223236 (RST, 2000) with an ER of 12″ (yellow circle), which best matches the position of GJ 1078; 4, 5, and 6 – regions of increased gamma-ray emission (Fig. 8a, b, c) the objects from which are listed in Table 6. We also note that the region of the X-ray source 1RXH J052349.5+223236 contains a star marked in Table 6 under number 7.

The description of the columns in Table 6 corresponds to that for Table 3.

Among the stars falling into the regions of gamma-ray emission exceeding the background level, objects 4.5 and 5.1 are of interest for which information on the effective temperature, radius, and luminosity is available. The averaged spectral type of the objects, determined from the information in the GAIA DR2 catalog on the color indices $G-G_{RP}$ and $G_{BP}-G_{RP}$, yielded the following results: K6.5V for 4.5 and K8V for 5.1.

8 The GL 851.1 region

The map for this object, presented in Sinitsyna et al. (2019, 2020), is a mirror image. Therefore, to overlay it on the optical image, it was rotated by 180° relative to the vertical axis (Fig. 9). The yellow circles are objects from the GAIA DR2 catalog. The star GL 851.1 is denoted by number 1. Its distance to the maximum of gamma-ray emission is 21 arcsec. The data for objects 2 and 3 from the GAIA DR2 catalog are given in Table 7. The description of the columns in Table 7 corresponds to that for Table 3.

Objects 2 and 3 are located at a distance of 2.3 arcsec from each other and fall into the region of weak gamma-ray emission associated with GL 851.1. The interest in them is due to the fact that object 3 is a dwarf, according to Stassun et al. (2019), with the averaged spectral class G2, according to the SDSS DR16 photometry data (Ahumada et al., 2020). Object 2 is also a star according to GAIA observations. A parallax and proper motions have been determined for it. However, in the case of determining the proper motion, there are significant errors. For pmRA = −0.320 angular millisec-

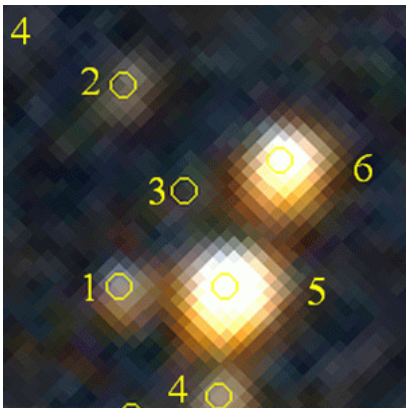

a) Map of region 4

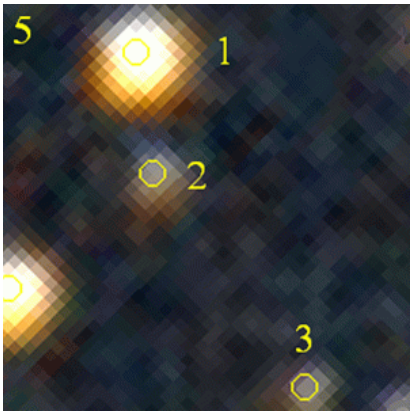

b) Map of region 5

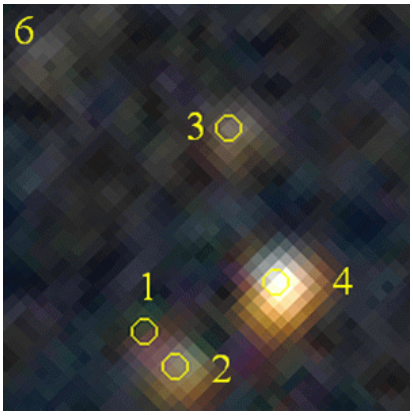

c) Map of region 6

Fig. 8.

Table 7.

No.	R.A. (2000)	Decl. (2000)	Plx	pmRA	pmDE	G	G_{BP}	G_{RP}	T_{eff}	Rad	Lum
2	333.03401553	+31.55554772	1.2811	−0.320	4.852	19.7206	20.2451	18.4217	–	–	–
3	333.03330817	+31.55555801	0.1898	0.057	−5.447	17.6793	18.0652	17.0552	–	–	–

onds per year, the error is 0.589, and for pmDE = 4.852, it is 0.821. The errors in determining the parallax are also significant: 0.4273 angular milliseconds. When using the 3σ criterion, the magnitude of the errors slightly exceeds the value of the determined parallax (3σ = 1.2819).

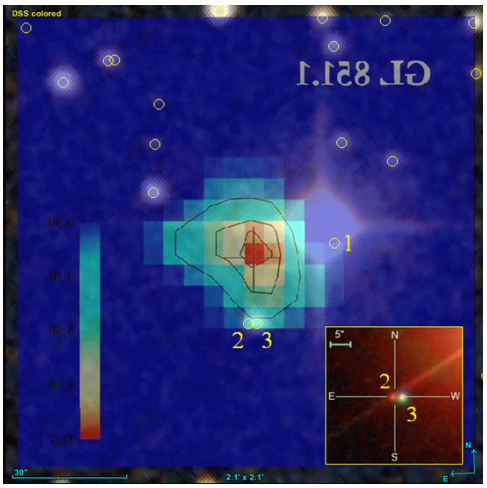

Fig. 9. Combined optical (DSS colored) and TeV images of the GL 851.1 region. The inset shows objects 2 and 3 in the SDSS atlas.

According to SDSS DR16 data, object 2 is a galaxy with a photometric (Oyaizu et al., 2008) redshift of 0.171 ± 0.1692. Significant errors in determining the redshift make us doubt in its reliability. It is possible, and this is clearly seen in the inset of Fig. 9, that the identification of object 2 as a galaxy is due to the projection of the diffraction beam from GL 851.1 and subsequent incorrect image processing.

9 The V780 Tau region

The maximum flux in the gamma-ray range is located at a distance of ~10 arcsec from the optical position of V780 Tau, denoted by number 1 in Fig. 10. All the objects from the GAIA DR2 catalog considered below are drawn with yellow circles. Taking into account the significant proper motion of V780 Tau, the star No. 3 occupies its position in the optical image of the region. V780 Tau itself has shifted lower and to the left at the epoch 2000.0. The data for objects falling into the regions of increased gamma-ray emission (marked with yellow rectangles) in the vicinity of V780 Tau are presented in Table 8. The description of the columns in Table 3 corresponds to that for Table 8.

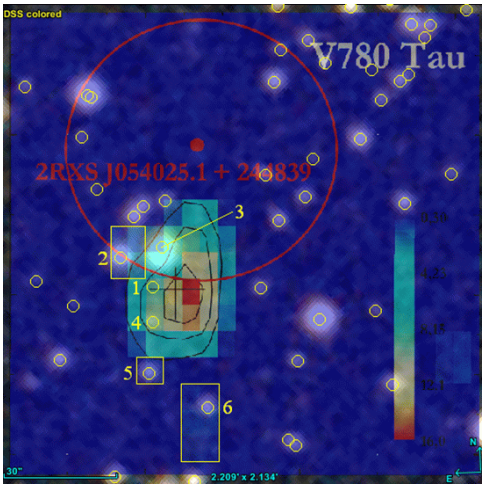

Fig. 10. Overlay of the gamma-ray isophote of the V780 Tau region on the optical image.

Table 8.

No.	R.A. (2000)	Decl. (2000)	Plx	pmRA	pmDE	G	G_{BP}	G_{RP}	T_{eff}	Rad	Lum
2	085.11024188	+24.80279535	0.2364	3.406	−1.215	16.0450	16.6976	15.2211	4332.67	–	–
3	085.10686509	+24.80357145	0.0514	1.992	−0.753	19.4176	20.1994	18.4724	–	–	–
4	085.10766325	+24.79806903	–	–	–	20.5223	21.0957	19.0595	–	–	–
5	085.10796446	+24.79425983	0.0066	2.105	−0.751	18.7862	19.4006	17.9025	–	–	–
6	085.10315316	+24.79172505	−0.0479	1.568	−0.873	18.5154	19.0813	17.5660	–	–	–

Table 9.

No.	R.A. (2000)	Decl. (2000)	Plx	pmRA	pmDE	G	G_{BP}	G_{RP}	T_{eff}	Rad	Lum
2	086.46128416	+22.88003290	8.9771	3.820	−37.943	12.9985	14.4091	11.8235	4078.39	0.61	0.093
3	086.46016711	+22.87969449	1.1031	2.352	−5.134	18.6179	19.0753	17.0258	–	–	–

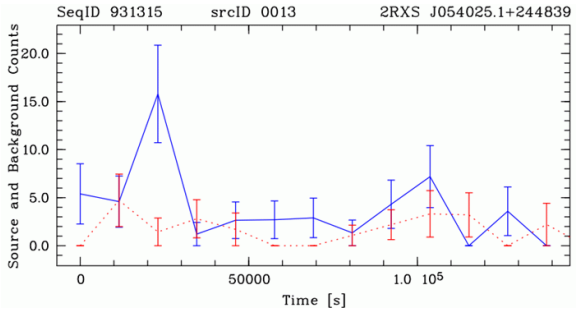

Fig. 11. Light curve of the object 2RXS J054025.1+244839 = V780 Tau in the X-ray spectral range. The axes show time from the start of observations in seconds and detector counts for the source (blue curve) and background (red curve). Measurement errors are indicated.

Under V780 Tau, number 6 denotes an object from GAIA DR2 (Gaia Collaboration et al., 2018) with G_{RP} of stellar magnitude $17^{m}.566$, which coincides in position with a weak detected gamma-ray flux (marked with a yellow rectangle). The star has coordinates $05^{h}40^{m}24^{s}.76$ +24°47′30″.2, and a parallax and proper motion have been determined for it. However, data from the IGAPS catalog (Monguió et al., 2020), obtained from observations with the Isaac Newton Telescope (INT) between 2003 and 2018, introduce uncertainty in the classification of the object as a star or galaxy.

We note that V780 Tau shows weak variability in the X-ray spectral range according to data from the second ROSAT source catalog (Boller et al., 2016). The change in the detected flux of 2RXS J054025.1+244839 over time is shown in Fig. 11.

10 The V962 Tau region

V962 Tau, denoted in Fig. 12 by number 1, is located at a distance of ∼10 arcsec from the maximum flux in the gamma-ray range. Data on objects falling into the region of weaker gamma-ray emission are presented in Table 9. The description of the columns in Table 9 corresponds to that for Table 3.

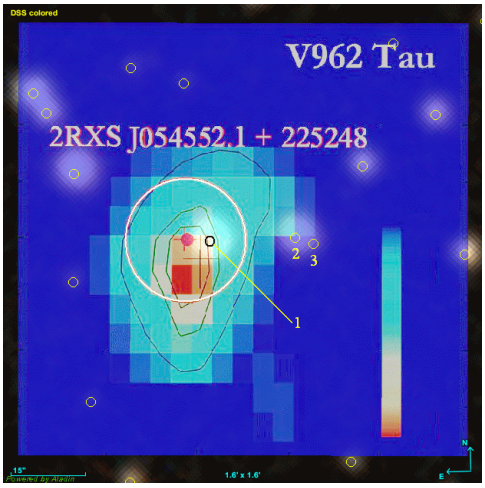

Fig. 12. Localization of the TeV source against the background of the optical image of the V962 Tau region.

11 Conclusions

As a result of the conducted analysis, we established a correspondence between TeV emission sources and red dwarf stars. It was suggested that other objects in the field, particularly X-ray sources 2SXPS J010321.2+622159 = 522864272037651712, 1RXS J052327.7+222649 = 3414565834307772672, and 2SXPS J054550.7+225249 = 3427527766435285248, could be identified in the optical spectral range. The unique designation for all GAIA data releases is indicated after the equal sign. Formally, Gaia DR2 should be placed before the designation.

A list of 39 objects falling into the regions of weak gamma-ray emission exceeding the background level and in the vicinity of the stars considered in Sinitsyna et al. (2019) and Sinitsyna et al. (2020) was compiled. It should also be noted that the coordinate support of the figures with the distribution of gamma-ray emission near the considered red dwarfs contains errors. This somewhat complicated the identification in the optical range.

Acknowledgments. During the work, we have actively used the SIMBAD, VizieR, and Aladin applications supported by the Strasbourg Astronomical Data Center, as well as the SAO/NASA ADS bibliographic service. The author is grateful to all who ensure their operation and expresses gratitude to the Russian Foundation for Basic Research for partial support of the conducted research through grants No. 19-02-00191 and No. 19-29-11027.

The author sincerely thanks M.M. Katsova for discussing the article and making useful comments.

References

Ahumada R., Prieto C.A., Almeida A., et al., 2020. Astrophys. J., Suppl. Ser. , vol. 249, no. 1, 3.

Alam S., Albareti F.D., Allende Prieto C., et al., 2015. Astrophys. J., Suppl. Ser. , vol. 219, no. 1, 12.

Alekseev I.Y., Chalenko N.N., Fomin V.P., et al., 1995. In J. Greiner, H.W. Duerbeck, R.E. Gershberg (Eds.), IAU Colloq. 151: Flares and Flashes. p. 78. doi:10.1007/3-540-60057-4_239.

Baird G.A., Delaney T.J., Lawless B.G., et al., 1975. Astrophys. J. Lett., vol. 196, pp. L11–L13.

Boller T., Freyberg M.J., Trümper J., et al., 2016. Astron. Astrophys., vol. 588, A103.

Bonnarel F., Fernique P., Bienaymé O., et al., 2000. Astron. Astrophys. Suppl. Ser., vol. 143, pp. 33–40.

Caballero-García M.D., Castro-Tirado A.J., Claret A., et al., 2016. In M.D. Caballero-García, S.B. Pandey, D. Hiriart, A.J. Castro-Tirado (Eds.), Revista Mexicana de Astronomia y Astrofisica Conference Series. Revista Mexicana de Astronomia y Astrofisica Conference Series, vol. 48, pp. 59–63 (arXiv:1512.07034).

Cavallo G., Jelley J.V., 1975. Astrophys. J. Lett., vol. 201, pp. L113–L115.

Costa E., Feroci M., Frontera F., et al., 1997. IAU Circ., vol. 6572, p. 1.

D'Elia V., Perri M., Puccetti S., et al., 2013. Astron. Astrophys., vol. 551, A142.

D'Elia V., Gehrels N., Holland S.T., et al., 2014. GRB Coordinates Network, vol. 16158, p. 1.

Evans P.A., Page K.L., Osborne J.P., et al., 2020. Astrophys. J., Suppl. Ser. , vol. 247, no. 2, 54.

Gaia Collaboration, Brown A.G.A., Vallenari A., et al., 2018. Astron. Astrophys., vol. 616, A1.

Gershberg R.E., Terebizh A.V., Shlyapnikov A.A., 2011. Bulletin Crimean Astrophysical Observatory, vol. 107, no. 1, pp. 11–19.

Giacconi R., Gursky H., Paolini F.R., Rossi B.B., 1962. Phys. Rev. Lett., vol. 9, no. 11, pp. 439–443.

Gorbachev M.A., Ignatov V.K., Shlyapnikov A.A., 2019. In A.V. Stepanov, Y.A. Nagovitsyn (Eds.), Solar and Solar-Earth Physics - 2019. pp. 115–118. doi:10.31725/0552-5829-2019-115-118.

Groot P.J., Galama T.J., van Paradijs J., et al., 1997. IAU Circ., vol. 6584, p. 1.

Gursky H., Giacconi R., Gorenstein P., et al., 1966. Astrophys. J., vol. 146, pp. 310–316.

Holt S.S., Ramaty R., 1969. Solar. Phys., vol. 8, no. 1, pp. 119–141.

Klebesadel R.W., Strong I.B., Olson R.A., 1973. Astrophys. J. Lett., vol. 182, p. L85.

Mamajek E., 2019. A Modern Mean Dwarf Stellar Color and Effective Temperature Sequence, Version 2019.3.22. Available at: https://www.pas.rochester.edu/~emamajek/EEM_dwarf_UBVIJHK_colors_Teff.txt.

Monguió M., Greimel R., Drew J.E., et al., 2020. Astron. Astrophys., vol. 638, A18.

Oyaizu H., Lima M., Cunha C.E., et al., 2008. Astrophys. J., vol. 674, no. 2, pp. 768–783.

Pecaut M.J., Mamajek E.E., 2013. Astrophys. J., Suppl. Ser. , vol. 208, no. 1, 9.

Peterson L.E., Winckler J.R., 1959. J. Geophys. Res., vol. 64, no. 7, pp. 697–707.

Sahu K., Livio M., Petro L., Macchetto F.D., 1997. IAU Circ., vol. 6606, p. 2.

Sandage A., Osmer P., Giacconi R., et al., 1966. Astrophys. J., vol. 146, p. 316.

Sinitsyna V.G., Sinitsyna V.Y., Stozhkov Y.I., 2019. In B. Pattison, Y. Itow, T. Sako, H. Menjo (Eds.), European Physical Journal Web of Conferences. European Physical Journal Web of Conferences, vol. 208, p. 14007. doi:10.1051/epjconf/201920814007.

Sinitsyna V.G., Sinitsyna V.Y., Stozhkov Y.I., 2020. In M. Nakahata (Ed.), Journal of Physics Conference Series. Journal of Physics Conference Series, vol. 1468, p. 012082. doi:10.1088/1742-6596/1468/1/012082.

Stassun K.G., Oelkers R.J., Paegert M., et al., 2019. Astron. J., vol. 158, no. 4, 138.

Voges W., Aschenbach B., Boller T., et al., 2000. IAU Circ., vol. 7432, p. 3.

Webb N.A., Coriat M., Traulsen I., et al., 2020. VizieR Online Data Catalog, IX/59.

Wenger M., Ochsenbein F., Egret D., et al., 2000. Astron. Astrophys. Suppl. Ser., vol. 143, pp. 9–22.